Available online at www.sciencedirect.com

ScienceDirect

Ceramics International 40 (2014) 1341–1350

CERAMICS INTERNATIONAL

www.elsevier.com/locate/ceramint

Effect of microstructure refinement on performance of $Ni/Ce_{0.8}Gd_{0.2}O_{1.9}$ anodes for low temperature solid oxide fuel cell

Fatemeh Sadat Torknik[a,*], Mansoor Keyanpour-Rad[a], Amir Maghsoudipour[a], Gyeong Man Choi[b]

[a]*Materials and Energy Research Center (MERC), P.O. Box 14155-4777, Tehran, Iran*

[b]*Fuel Cell Research Center and Department of Materials Science and Engineering, Pohang University of Science and Technology (POSTECH), Pohang 790-784, South Korea*

Received 2 June 2013; accepted 1 July 2013
Available online 8 July 2013

Abstract

To clarify the role of milling process on polarization resistance of Ni/GDC cermet anodes for low temperature solid oxide fuel cell (LT-SOFC), an anode with the structure of $NiO/Ce_{0.8}Gd_{0.2}O_{2-\delta}$ (NiO/GDC20) was prepared via two different milling processes, including conventional ball-milling (CBM) and high energy ball-milling (HEBM). NiO/GDC20 anode composites were fabricated by screen-printing of the milled powders on the dense sintered GDC electrolyte substrate. By employing electrochemical impedance spectroscopy analysis, the effect of the milling process intensity on the LT-SOFC anode performance was examined using a symmetric Ni–GDC20/GDC20/Pt electrolyte-supported cell at 400–600 °C. Microstructural studies of NiO/GDC composite powders showed effectiveness of HEBM method on disintegration of CBM aggregates. HEBM powder with much finer particle size showed smaller crystallites than the CBM powder, which led to a finer-grained uniformly-distributed Ni/GDC anode microstructure. In comparison with the anode prepared by CBM powder, the resulted cermet anode showed further GDC lattice expansion, lower anodic polarization resistance, and also decreased activation energy for hydrogen oxidation reaction. Detailed anode impedance analysis showed dominant role of the charge transfer process and rate determining step of dissociation/adsorption/diffusion in hydrogen-oxidation reaction of both Ni/GDC anodes. In addition, evaluation of activation energy showed enhancement of the charge transfer and dissociation/adsorption/diffusion steps with finer-grained microstructure. It is found that the refinement of microstructure has a significant role on the anode polarization resistance and related electrochemical processes.
© 2013 Elsevier Ltd and Techna Group S.r.l. All rights reserved.

Keywords: LT-SOFC; Ni/GDC anode; High energy and conventional ball-milling; Microstructure

1. Introduction

Ceria doped with rare-earth oxides, especially gadolinium doped ceria (GDC) due to high oxygen ion conductivity below 600 °C, is a promising component material used as electrolytes and anodes in intermediate- and low-temperature solid oxide fuel cell (IT- and LT-SOFC). Thermal expansion coefficient of GDC is much close to that of nickel-cermets and commercial ferrite stainless steel interconnects. The addition of electronic–ionic conductor ceramic phase, such as GDC, to nickel in order to make Ni-cermet, offers decreased anode overpotential and electrical resistance, limited nickel agglomeration at high temperature, increased active electrode thickness, and also matched anode thermal expansion coefficient to that of the ceramic electrolyte. Therefore, Ni/GDC cermet anode is considered to be a promising candidate for the LT-SOFC applications where high activity and electrical conductivity and relatively low cost are required [1–4].

Nowadays, milling as a mature technique is used for size reduction of solid particles, mixing and combination of chemical

*Corresponding author. Tel.: +98 9121886748; fax: +98 2188773352.
E-mail addresses: fstorknik@gmail.com, fstorknik@yahoo.com (F.S. Torknik).

0272-8842/$ - see front matter © 2013 Elsevier Ltd and Techna Group S.r.l. All rights reserved.
http://dx.doi.org/10.1016/j.ceramint.2013.07.015

elements down to the atomic scale, and initiation or acceleration of solid state chemical reactions [5]. In comparison with conventional ball-milling (CBM), high-energy ball milling (HEBM) is considered to be more efficient in modifying the particle morphology of materials [6]. Due to the kinetic energy resulted from the collisions of particles, balls and bowl, HEBM does not only break down the powder particles into fine pieces, but also enables the powder to mix properly. Therefore, an extremely fine and homogeneously mixed composite powder is produced which leads to high sintering activity and superior mechanical properties [7].

It is well documented that the method of simple mechanical mixing of separately prepared NiO and GDC powders [8] to form Ni/GDC cermets, leads to accurate chemical composition [9]. A large number of studies have been performed on the fabrication and characterization of Ni/GDC anodes using CBM [8,10–12]. However, the application of the HEBM and its effect on microstructure development of NiO/GDC composite powder for fabricating Ni/GDC anode, have not been reported in the literature. Recently, Lee et al. [13] have only utilized planetary milling to prepare NiO/GDC powder to study the $GdBaCo_2O_{5+x}$ cathode for anode-supported ceria SOFCs. Cho et al. [14] also have used HEBM process to prepare NiO/Y_2O_3-stabilized ZrO_2 (NiO/YSZ) composite powder for high temperature (800 °C) SOFC anode. They have shown uniform distribution of particles of Ni in the Ni/YSZ pressed pellets and consequently good performance at 800 °C for the anode, was resulted.

Microstructure of the material which is due to composition and fabrication conditions strongly affects the Ni/GDC composite anode performance [8]. In comparison with Ni/GDC anodes prepared by CBM, further improvements in the Ni/GDC anodic property would be obtained if a homogeneous and contiguous structure of pores and Ni and GDC fine grains are developed. Hence, further enlargement of the three-phase boundaries (TPBs) of Ni/GDC composite anode is obtained [9]. Consequently, extension of the TPB length due to its correlation with the reaction rate of H_2 electrochemical oxidation, improves anode performance [15]. In this paper, to clarify the role of the milling process in Ni/GDC cermet anodes for LT-SOFC, a comparison was made between microstructural development and performance of Ni/GDC anodes prepared by HEBM and CBM methods. The NiO/GDC powders were applied by the screen-printing method on the dense sintered GDC electrolyte substrate. The hydrogen oxidation reaction mechanism was investigated by using electrochemical impedance spectroscopy (EIS) in constant parameters of cell design, electrode material, fuel type, and working temperature. The performance of Ni/GDC anodes was examined by the electrolyte-supported symmetric Ni–GDC20/GDC20/Pt cells for LT-SOFC to obtain an appropriate substrate.

2. Experimental procedure

GDC20 ($Gd_{0.2}Ce_{0.8}O_{2-\delta}$) powder was synthesized by the solid-state reaction of Gd_2O_3 and CeO_2 (both with purity of 99.9%, High Purity Chemicals, Japan) [16] with mean particle sizes of 3.9 μm and 10 μm, respectively. The calcined GDC20 was ball-milled in ethanol for 24 h. Electrolyte substrates were prepared by tape casting [17] of 10 h-planetary milled GDC20 powder. The green tapes were sintered at 1400 °C in air for 5 h. The GDC20 electrolytes with 15 mm diameter and ~0.3–0.4 mm thickness were obtained with higher than 93% of theoretical density. NiO–GDC20 powder was synthesized using NiO powder (Kojundo Chemical, 99.97%, Japan) with d_{50} of 1.8 μm and aforementioned ball-milled GDC20 powder in a weight fraction of 0.6:0.4, respectively. Milling was performed in ethanol in a polypropylene jar with zirconia balls (5 and 10 mm) for 24 h. The milling speed and ball-to-powder ratio was 100 rpm and 4.8:1, respectively. The ball-milled NiO–GDC powder (denoted with NG-B) was milled using a planetary mill (PM) to decrease particle size for comparing with NG-B (denoted with NG-P). Milling was carried out in a planetary mono mill (Fritsch, Pulverisette 6 classic line, Germany) in ethanol in an 80 cc zirconia bowl with zirconia balls (1 mm diameter) for 2 h. The milling speed and ball-to-powder ratio was 500 rpm and 2.8:1, respectively. In order to study the anode performance, the NiO_{60}–$GDC20_{40}$ composite powders were used as precursors of the anode screen printing for LT-SOFC half-cells. The powder was mixed with screen-printing solution [18] (in a weight ratio of 1:1) and dihydroterpineol acetate (DHTA) and BYK-103 as the dispersants, followed by homogenizing and screen printing through a 200-size mesh in a circular shape with 0.5 cm^2 area on the center of the GDC20 electrolyte disc. Sintering was performed at 1300 °C and also at 1350 °C in air for 2 h to attain an appropriate porous microstructure with ~15 μm thickness.

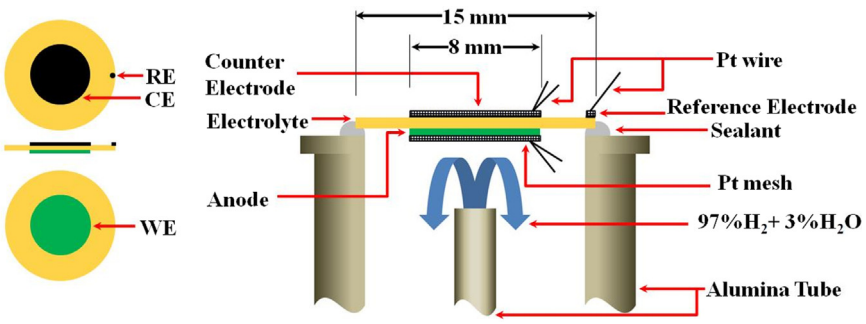

Fig. 1. Schematic configuration of the cell for impedance test of Ni/GDC anodes.

The anodic impedance was tested in two-chamber conditions, using a three-electrode array, as shown in Fig. 1. Pt paste (no. 6082, Engelhard) was used in painting of the counter and reference electrodes, symmetrically opposite to the working electrode and a small point at the electrolyte edge with 3 mm-distance from the counter electrode, respectively. Also Pt mesh (52 mesh, Alpha Aesar) was used as a current-collector in intimate contact with the electrodes. Before testing, NiO was reduced in situ at 600 °C for 1 h. The impedance spectra of the cermet anode were collected using an LF impedance analyzer (4192A, Hewlett-packard) under open circuit potential with amplitude of 0.01 V in the frequency range 10 Hz–1 MHz at the temperature range of 400–600 °C (50 °C steps). Humidified hydrogen (3 vol% H_2O) was used as the fuel gas with flow rate of 80 cc/min and open air as the oxidant. R type thermocouple was used for measuring precise temperature close to the anode. The impedance data were analyzed using the ZView software (version of 3.1, Scribner Associates, Southern Pines, NC, US), considering a value of chi-squared, χ^2, of E^{-3}–E^{-4}.

The granulometric analysis of the original and the milled powders was carried out using laser-based analyzer of Horiba partica LA-950v2 with ultrasonic treatment. X-ray diffraction (XRD) was measured using a PW3710 Philips diffractometer with Co Kα radiation ($\lambda = 1.790307$ Å) and a D/Max-2500/PC Rigaku diffractometer with Cu Kα radiation ($\lambda = 1.540598$ Å). The inner microstructure of the milled powders and the composites, namely the average crystallite size and lattice strain, and the lattice parameter was investigated. This was done by applying the Williamson and Hall method [19] from the broadening (FWHM) of the first three/four diffraction lines (111, 200, 220, and 311) with regard to the instrumental broadening effect. Scanning electron microscopy (SEM, Philips XL30S FEG) was used to evaluate the morphology of the powders and microstructure of the anodes before and after H_2 reduction and after the EIS measurement. Average particle size and porosity of the anode were determined, using Digital Micrograph software from 100 particles as minimum and image J 1.45s software, respectively.

3. Results and discussion

3.1. Microstructures of the milled powders

Fig. 2(a and b) shows SEM micrographs of the milled powders. It is seen that the NG-P composite powder shows finer equiaxed agglomerates compared to NG-B composite powder which has coarse disordered morphology. Fig. 2c shows laser granulometry analysis plot of the milled composite powders compared with the original powders (OPs) after 1 and 5 min ultrasonic treatment. Table 1 summarizes mean size and d_{50} of the powders. 5 min-ultrasonic disintegrates the soft agglomerates but it is too short to the same thing to aggregates.

Evaluation of the OPs indicates that NiO, due to disappearance of the large tail of 50–200 μm and achievement of an ultimate bimodal distribution, includes more soft agglomerates. In contrast, the non-uniform unimodal size distribution of the coarse GDC aggregates shows stronger necks caused by the conventional ceramic method. Comparison of the milled powders with the OPs shows that reduction of particle size depends on the milling process intensity. The lack of significant change on wide size distribution of the NG-B powder, indicates that CBM intensity is somehow capable to destruct

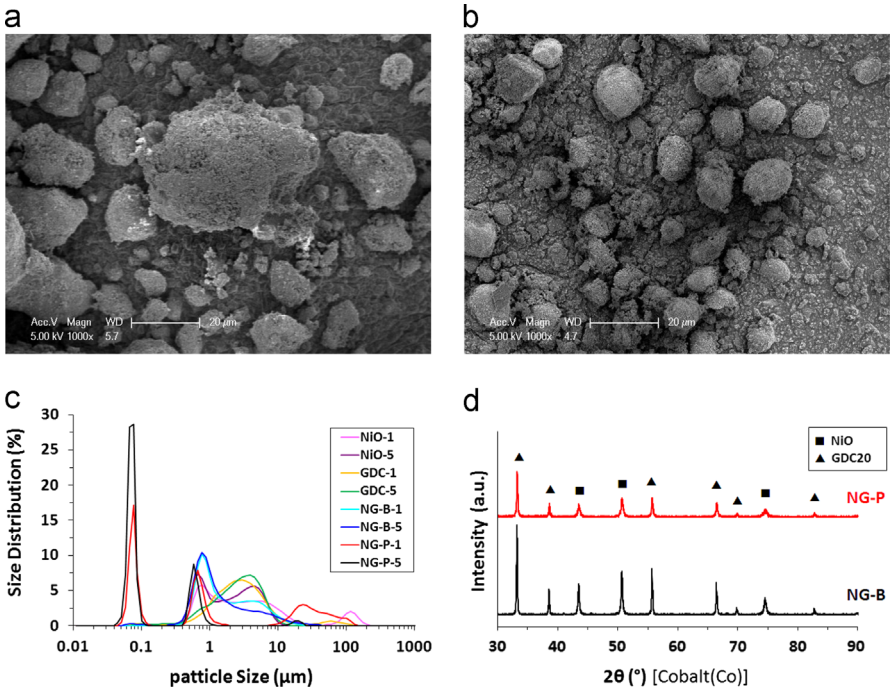

Fig. 2. (a) SEM micrograph of NG-B powder, (b) SEM micrograph of NG-P powder, (c) Granulometry analysis of NiO, GDC20, NG-B and NG-P powders recorded after 1 min and 5 min ultrasonic treatments and (d) XRD pattern of NG-B and NG-P powders.

Table 1
Particle mean size and d_{50} of the milled and original powders.

Material	Mean particle size (d_{50}) (μm)	
	after 1-min ultrasonic	after 5-min ultrasonic
NG-B powder	2.46 (1.22)	2.37 (0.98)
NG-P powder	11.80 (0.59)	0.55 (0.07)
NiO powder	13.72 (2.39)	2.46 (1.78)
GDC powder	5.48 (2.54)	2.90 (2.49)

Table 2
Average grain size (D), lattice microstrain (ε) and lattice parameter (a) of the milled powders.

Material	NiO			GDC		
	D (nm)	ε (%)	a (Å)	D (nm)	ε (%)	a (Å)
NG-B powder	105	0.32	4.1816	93	0.01	5.4236
NG-P powder	49	0.65	4.1782	58	0.02	5.4137

the large aggregates. On the contrary, disappearance of the 10–100 μm large tail, compensate considerable increase of the peak intensity of the most frequent particle size (~0.07 μm) on bimodal distribution of the NG-P powder, implying fracture of the building blocks of NG-B powder. As a result, ability of PM to destruct the intra-agglomerate structure of the aggregates to ingredients with one or two order of magnitude smaller in size, even into nanometer scale could be rationalized that morphological evolution of the ground powders depends strongly on the mechanical properties of the components of the initial mixture, especially the Young's modulus (E_{NiO}=95.8 GPa [20] or E_{NiO}=171.8 GPa [21] and E_{GDC}=212.2–216.6 GPa [22]).

It is noteworthy that crystallite size of the particles is not generally the same as the particle size due to the presence of polycrystalline aggregates. Fig. 2d shows XRD patterns of the NG-B and NG-P powders. Average crystallite size (D), lattice strain (ε) and lattice parameter (a) of cubic NiO and GDC20 phases in the milled powders are listed in Table 2. The small peak shift to higher angles in XRD pattern of NG-P powder (proportion to NG-B powder) is related to decrease of the lattice parameter and can be attributed to the planar defects and also to solubility limit of <1 mol% for NiO in GDC [23]. The results indicated that NG-P powder grain size decreases coupled with an increase in strain when milled by PM (Table 2). Due to mechanical milling, NiO and GDC powders are exposed to high mechanical stresses in the range of microseconds. The powder particles without any change in their composition, endure the structural changes like reduction in grain size (53% for NiO and 38% for GDC) and development of plastic inhomogeneous strain (~100%). In light of the effect of milling intensity on the microstructural evolution, it is expected that smaller mean size of NG-P powder leads to high sinterability [24], increasing the anodic reaction rates and consequently improvement of the anode performance.

3.2. Microstructure of the sintered composites

Fig. 3 shows the microstructure of NiO/GDC composites made of NG-B and NG-P powders after sintering at 1300 °C and 1350 °C. This figure shows the formation of coarse pores which are required to facilitate the transport of reactant and product gases. The roughening in Fig. 3c and d can be attributed to the gas produced by the decomposition of the screen printing solution of organic constituents before sintering of the particles [12]. The network-structure development of composite particles is different depending on the internal structures of the particles. According to Fig. 3a, a distinct granular type of morphology with insufficient isolated sintering necks among NiO and GDC aggregates is obtained from the sintering of NG-B powder at 1300 °C. Inset in Fig. 3a shows the intra-particle necks of a typical GDC aggregate in point-to-point connection to other particles. Sintering temperature of 1350 °C induces significant enhancement in connectivity of the particles as face-to-face type which results from an improved material diffusion [25] (Fig. 3b). It is found that promotion of contact between NiO and GDC particles can be contributed in TPB length extension [24]. The morphological evolution of NG-P powder resulted in an anode microstructure with well established connections between homogeneously distributed small particles, as seen in Fig. 3(c and d). The microstructure of NG-P composite is still very fine after sintering at 1350 °C. Although higher sintering temperature is preferable due to the mechanical strength improvement [3], but the significant densification (>1380 °C) [12] and pronounced grain growth at higher sintering temperature caused by over-connection of sintering necks [24] and decrease in activity of the electrode due to decrease in the surface area [3]. It is found that to attain a high TPB value, average particle size of both phases should remain as small as possible. Also for obtaining suitable electrical properties, the contact between the

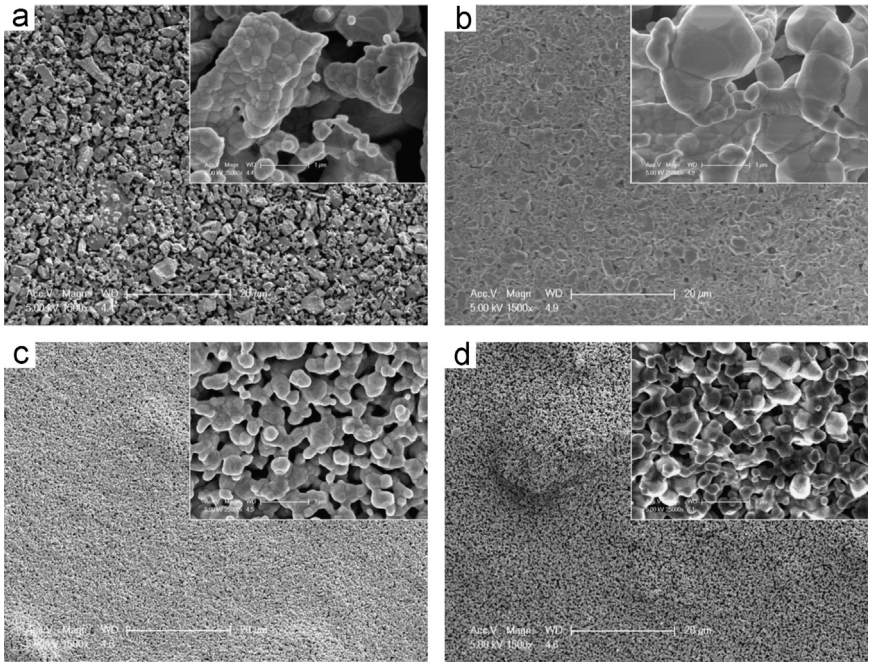

Fig. 3. SEM micrographs of sintered surface (top-views) of NiO/GDC composites fabricated by using: NG-B powder after sintering at (a) 1300 °C and (b) 1350 °C, NG-P powder after sintering at (c) 1300 °C and (d) 1350 °C.

Table 3
Grain size (*D*), lattice strain (*ε*) and lattice parameter (*a*) of the sintered composites.

Material	**NiO**			**GDC**		
	D (nm)	***ε*** **(%)**	***a*** **(Å)**	***D*** (nm)	***ε*** **(%)**	***a*** **(Å)**
NG-B sintered	362	0.13	4.1773	290	0.20	5.4162
NG-P sintered	132	0.005	4.1795	145	0.07	5.4231

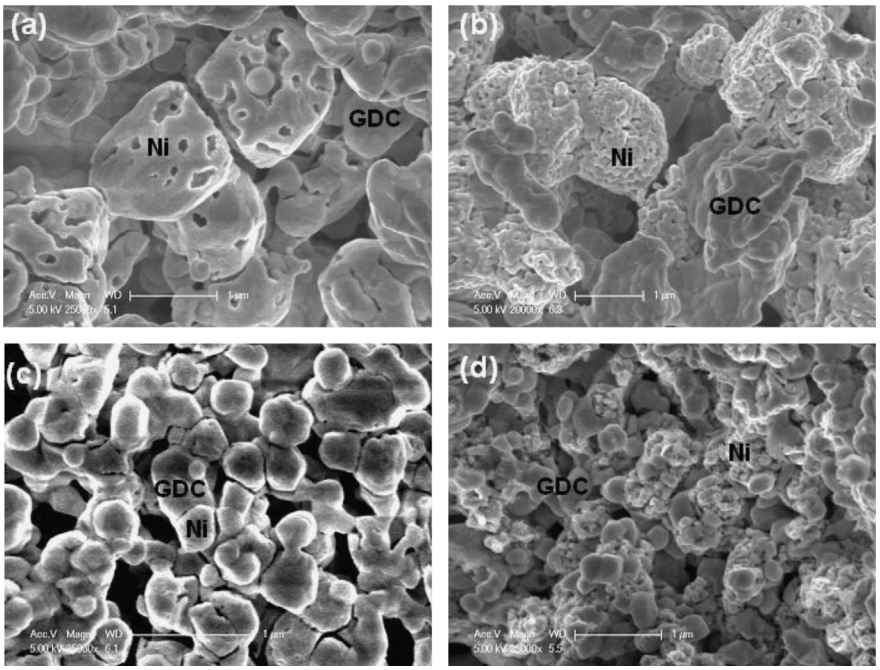

Fig. 4. Micro-scale fractured cross-sectional SEM images of the reduced Ni/GDC anodes fabricated by using NG-B powder (a) before and (b) after testing, NG-P powder (c) before and (d) after testing.

particles should be adequate, consequently the subsequent studies are carried out on the 1350 °C sintered composites. Microstructural inspection shows that the average particle size and the porosity in NG-B and NG-P composites are 0.38 μm and 0.30 μm, and 36% and 34%, respectively. Based on much faster TPB length enhancement of the small particles in the early sintering stage [24], it is predictable that because of improving TPB [9], NG-P composite further enhances the anodic performance.

The result of microstructural evaluation, including grain size, lattice strain and lattice parameter extracted from XRD spectra of the NG-B and NG-P sintered composites are listed in Table 3. The considerable grain growth in NG-B composite can be attributed to the inter-particle diffusion [26] of the adjacent grains in the aggregates (inset in Fig. 3b). Homogenous distribution of particles (inset in Fig. 3d) including finer grains in NG-P composite results in less coarsening due to the slight surface-diffusion.

The phases in the sintered composite of NG-P show much lower strain than that of NG-B composite. So sintering provides the required activation energy for releasing part of the residual stresses stored in the material causing relaxation of lattice/grain boundary [27]. Hence, the variation of the unit cell parameters is interpreted in terms of grain surface relaxation. In addition, the increase in GDC strain and the decrease in NiO strain with reference to the milled powders (Table 2) are found. It is believed that crystallite strain in the sintered phases is a measure of distribution of lattice constants arising from crystal imperfections, such as point defects, grain boundaries, especially triple junctions and sinter/contact stresses between adjacent particles [28].

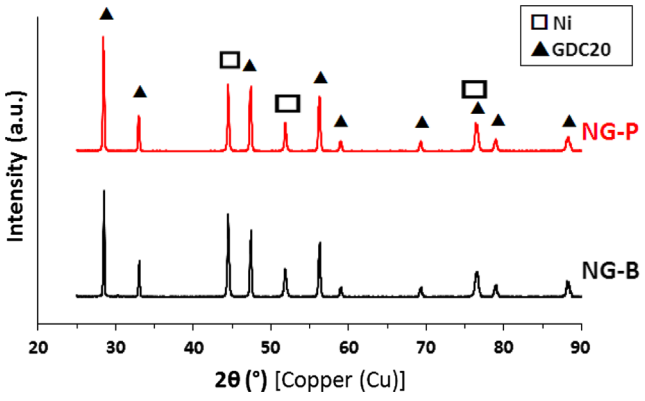

Fig. 5. X-ray diffraction pattern of NG-B and NG-P cermet anodes.

3.3. Microstructure of the anodes

The microstructure of Ni/GDC cermets of NG-B and NG-P after reduction in flow of H_2 for 1 h, is shown in Fig. 4(a and c). The reduction of NiO to Ni, causes an overall ~40% shrinkage in volume [4] and leaves a nanoporous material [29]. Fig. 4a shows clearly the formentioned mesopores (2–50 nm) and voids which are localized around and in the Ni particles, indicating that commencement of the NiO reduction as an autocatalytic reaction is at the NiO/GDC interfaces and proceeds to the center of the grain [29]. Microstructural analysis shows that the porosity in NG-B and NG-P cermets enhances to 42% and 43%, respectively.

The X-ray diffraction pattern of NG-B and NG-P cermet anodes is depicted in Fig. 5. Also, the XRD extracted data of Ni/GDC cermet anodes are listed in Table 4. The results indicate a 4–5 times decrease in Ni grain size and an increase in Ni lattice strain relative to the NiO phase in the sintered composites. Increment of the strain could be the result of the nickel coarsening and also remaining NiO [29]. By decreasing the grain size of Ni and GDC in NG-P anode, the contact sites of Ni and GDC enhance [30], consequently the length of TPB increases exponentially based on the theoretical studies [31]. A much larger increase of the GDC lattice parameter in NG-P cermet (0.25%) than that in NG-B cermet (0.06%) can be rationalized by the lattice expansion due to Ce^{4+} reduction to Ce^{3+} [2] and mutual diffusion in nearby smaller Ni and GDC grains of NG-P cermet, which is parallel to work recently done in the literature [32]. Finally, deviation in the lattice parameter can be diminished by the grain surface relaxation effect [33]. It is expected that the lower grain size and strain of Ni and GDC phases beside of the relative grain size in NG-P cermet anode, can facilitate electron and O^{-2} conductivity more effectively than NG-B anode.

After experiencing impedance test, Ni/GDC cermet anodes showed a well-formed interface with the electrolyte. Fig. 4(b and d) shows the fractured cross-sectional SEM images of the Ni/GDC anodes after about 8 h exposure to the testing temperatures of 400–600 °C. The porosity of the Ni/GDC anodes exhibits a slight increase (44% and 44.5% for NG-B and NG-P anode, respectively) than the reduced cermets, whereas the mean pore size of the NG-B cermet anode with polydispersed particle size [24] is larger than that for NG-P cermet. It can be deduced that due to the deterrent role of Ni sintering in the access/egress of H_2 gas to the Ni/NiO interface, complete reduction of the NiO is carried out during the cell testing.

Table 4
Grain size(D), lattice strain(ε) and lattice parameter (a) of the reduced cermet anodes.

Material	Ni			GDC		
	D (nm)	ε (%)	a (Å)	D (nm)	ε (%)	a (Å)
NG-B reduced	66	0.36	3.5255	362	0.18	5.4198
NG-P reduced	30	0.11	3.5235	207	0.17	5.4369

It could be noticed that a much finer-grained and homogeneous porous microstructure in NG-P anode is obtained than in the NG-B anode which the Ni phases are dispersed uniformly in the anode. The GDC particles, due to the non-vulnerability specification of bulk (up to 750 °C) [34] and out-diffuse of the crystallized Ni of the GDC grains [2] can be easily distinguished from Ni agglomerates (Fig. 4b and d). The average GDC particle size for NG-B cermet anode is 418 nm, less than double of 219 nm for NG-P anode. Similarly, a twofold coarsening of the metallic Ni particles can be observed in NG-B anode (645 nm) relative to NG-P anode (316 nm) due to a poor adhesion of the Ni metal to the GDC ceramic material at the operating temperatures. Finer grains of GDC with uniform dispersion in NG-P anode (as typically shown in Fig. 4d) hinder the destructive grain growth of Ni during cell-testing. Therefore, less coarsening of Ni and reduction of lattice strain of Ni and GDC phases (Table 4), are considered to be rationale to the preservation of extended TPBs in NG-P anode than NG-B anode. Accordingly, further enhancement of TPBs [9] is expected to improve the anode performance.

3.4. Performance of the anodes

The impedance response of the H_2 oxidation reaction on the Ni/GDC cermet anodes is characterized with no clear separation in the studied impedance frequency range. Fig. 6 shows the Cole–Cole Plot of impedance spectra for the H_2 oxidation reaction on the Ni/GDC cermet anodes in humidified H_2 at 600 °C. It can be seen that the NG-P anode shows low anodic polarization resistance (R_a=0.64 Ω cm^2) than that of the NG-B anode (R_a=0.98 Ω cm^2), namely a reduction of 35% in R_a value. Comparing the R_a values of the electrolyte-supported half-cells for the H_2 oxidation reaction at 600 °C, it is clear that

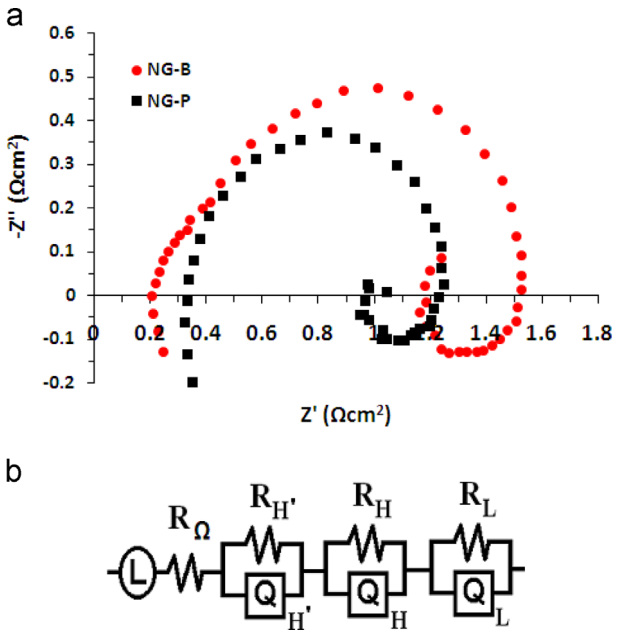

Fig. 6. (a) Anode impedance spectra for the H_2 oxidation reaction on the Ni/GDC cermet anodes of NG-B and NG-P measured in 97% H_2/3% H_2O at 600 °C. (b) Equivalent circuit.

the estimated R_a for the Ni/GDC anode attached to the YSZ-electrolyte [35] is ~7.5 Ω cm^2, is much larger than R_a values in this study. The R_a of the Ni/GDC anode attached to the GDC2AlCu-electrolyte [36], is ~1.5 Ω cm^2, more than 1.5 times of R_a value for the NG-B and NG-P anodes, respectively. The R_a value of NG-B and NG-P anodes is comparable to that of the symmetrical anodes made from NiO–GDC nanocomposite powder synthesized by mechanical (1.75 Ω cm^2) and chemical (0.63 Ω cm^2) methods [30], in addition to the R_a values of Ni/GDC anodes without (1.37 Ω cm^2) and with carbon (0.55 Ω cm^2) [37], respectively. The R_a evaluation can highlight the microstructural refinement effect on performance of the Ni/GDC composite anode.

Two inductive loops (negative section of spectra below the Z' axis) are characterized in the impedance response of the Ni/GDC anode (Fig. 6) at low and extra-high frequency besides a capacitive loop at high frequency. The low frequency inductive loop (or negative capacitive) is correlated to low polarization point on the I–V curve based on the simulated impedance in the case of heterogeneous reactions, while at high polarization point, it is converted to a capacitive loop [38]. The extra-high frequency inductive loop is most likely related to the closely spaced conductors, such as platinum wire current collectors and electric heating elements of the furnace that is commonly observed for the impedance responses of the SOFC electrodes. Unwanted stray impedances due to mutual inductance and stray capacitance in the geometrical set-up are particularly problematic at high frequencies and because of the small signal value of impedance at higher temperatures, it has much effect on the impedance pattern. Hence curve fitting at lower temperatures (T≤550 °C) should be more reliable.

The evaluation of impedance responses of the Ni/GDC anodes at testing temperatures shows that the R_a value for the NG-P anode is considerably less than that for the NG-B anode (Table 5). Also, the concurrent shift of the characteristic frequency to the lower frequency in Bode plot, apparently indicates the elimination of the surface inhibiting species on the NG-P anode surface than NG-B anode. Fig. 7 depicts shift characteristic frequency (indicated by the arrow) from about 120 kHz for NG-B anode to around 40 kHz for NG-P anode at 550 °C. The appearance of the diffuse peak of NG-B anode is most likely an indication of the increasingly dominant role of the high frequency processes.

In order to determine the origin of the difference in the anodes behavior, the interpretation of impedance curves is conducted based on the equivalent circuit of $LR_\Omega(RQ)_{H'}(RQ)_H(RQ)_L$ [39], (Fig. 6b), where L is the inductance of wiring and instruments, R_Ω is the ohmic resistance between anode and the reference electrodes. The series connection (subcircuits) of ($R_{H'}$, $Q_{H'}$), (R_H, Q_H) and (R_L, Q_L) corresponds to the extra-high, high and low frequencies, respectively and R_i is the resistance and Q_i is the constant-phase element (CPE). The Nyquist diagrams will be better interpreted if CPEs were replaced with pure capacitors in inhomogeneous surface. The CPE is generally associated with material inhomogeneity, electrode roughness or porosity, and with ionic transport deviations from Fick's law. The extra-high frequency subcircuit is most likely related

Table 5
Anode polarization resistance, R_a, $R_{H'}$, R_H, and R_L, for the H_2 oxidation reaction on the NG-B and NG-P anodes.

Temperature (°C)	Anode polarization resistance			
	R_a (Ω cm^2)	$R_{H'}$ (Ω cm^2)	R_H (Ω cm^2)	R_L (Ω cm^2)
NG-B				
550	5.52	0.51	5.43	1.56
500	48.25	1.09	44.59	4.73
450	309.84	1.53	199.6	113.1
400	989.83	2.63	666.2	324.6
NG-P				
550	3.96	0.32	3.47	0.84
500	37.96	0.40	24.31	14.29
450	181.36	0.49	123.8	52.84
400	268.62	2.95	153.2	108.3

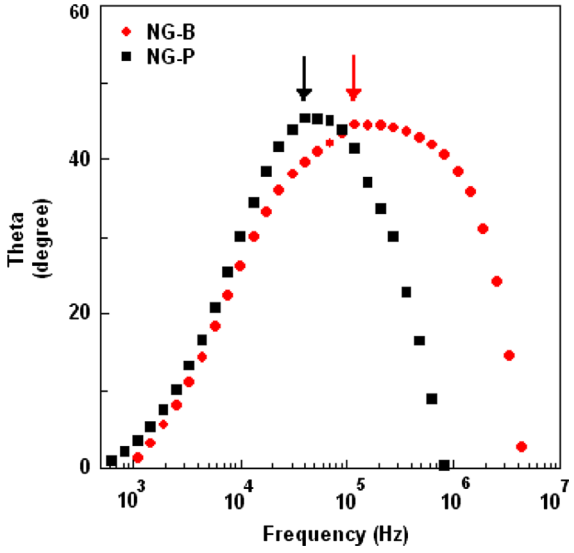

Fig. 7. Bode plot of impedance response for the H_2 oxidation reaction on the Ni/GDC cermet anodes of NG-B and NG-P in 97% H_2/3% H_2O at 550 °C.

to O^{-2} conduction/migration related to the electrolyte or anode/electrolyte interface. The high frequency segment is associated with the charge transfer process at the TPBs. The low frequency element is connected to the surface exchange including the adsorption, dissociation, and diffusion intermediates on the Ni/GDC surface. Validation of the aforementioned equivalent circuit is restricted only to lower temperature of 650 °C [35]. The equivalent circuit analysis of the impedance spectra for NG-B and NG-P anodes are summarized in Table 5. The results indicate that in both the anodes, the R_H has a dominant contribution in the total anode resistance (at least more than 57% of the total R_a), indicating that H_2 oxidation reaction on Ni/GDC cermet anodes is principally governed by the high frequency electrode process, while the role of R_L is not considerably important at higher temperature and enlarges by temperature lowering. This result is in contrast to the study of Ni/GDC anode attached to YSZ electrolyte over the high temperature range of 650–900 °C, indicating that the impedance curve for hydrogen oxidation reaction is mostly formed by R_L [40].

Fig. 8 shows the anode polarization resistance corresponding to R_a, $R_{H'}$, R_H, and R_L, in Arrhenius form for the NG-B and NG-P anodes in order to calculate the activation energy which listed in Table 6. The activation energy for the reaction on NG-P cermet anode becomes 1.33 eV, approximately 20% smaller than 1.65 eV on NG-B anode. Also, a decrement in the activation energy of the electrode processes related to R_H and R_L (less than 20%) which is coherent with R_a on NG-P anode. This is indicating that the electrochemical activity of the anode can be further enhanced by microstructural refinement of the cermet. The larger activation energy of R_L relative with respect to R_H in both the anodes, indicates that the reaction associated with the absorbed charged species is slower than the ordinary charge transfer process. According to Fig. 8b, by temperature lowering, $R_{H'}$ for NG-P anode remains approximately the same, whereas at temperature of 400 °C, an increase of one order of magnitude is noticed. In contrast, variation of $R_{H'}$ for NG-B anode even to 400 °C is roughly linear. The virtual enlargement of activation energy in NG-P anode than NG-B anode (36% in Table 6) is attributed to the variation of ion conductivity activation energy of GDC at $T \leq 400$ °C [41] based on the superstructure formation at the grain boundary of Ni and GDC grains [32] and critical role of the grain boundary in the low temperature range.

4. Conclusions

Microstructural studies of the NG-B and NG-P powders showed effectiveness of the planetary milling method on disintegrating of the ball-milled aggregates. The resulting NG-P powder with finer particle size exhibited smaller crystallite size and higher strain. Comparison of the NG-P and NG-B anodes together indicated that a finer-grained homogeneously-distributed microstructure with further lattice expansion of the GDC phase and lower anode polarization resistance for NG-P anode was resulted. Detailed anode impedance analysis indicated dominant role of the charge transfer process in hydrogen oxidation reaction in both Ni/GDC anodes. The decrement of the activation energy for hydrogen oxidation

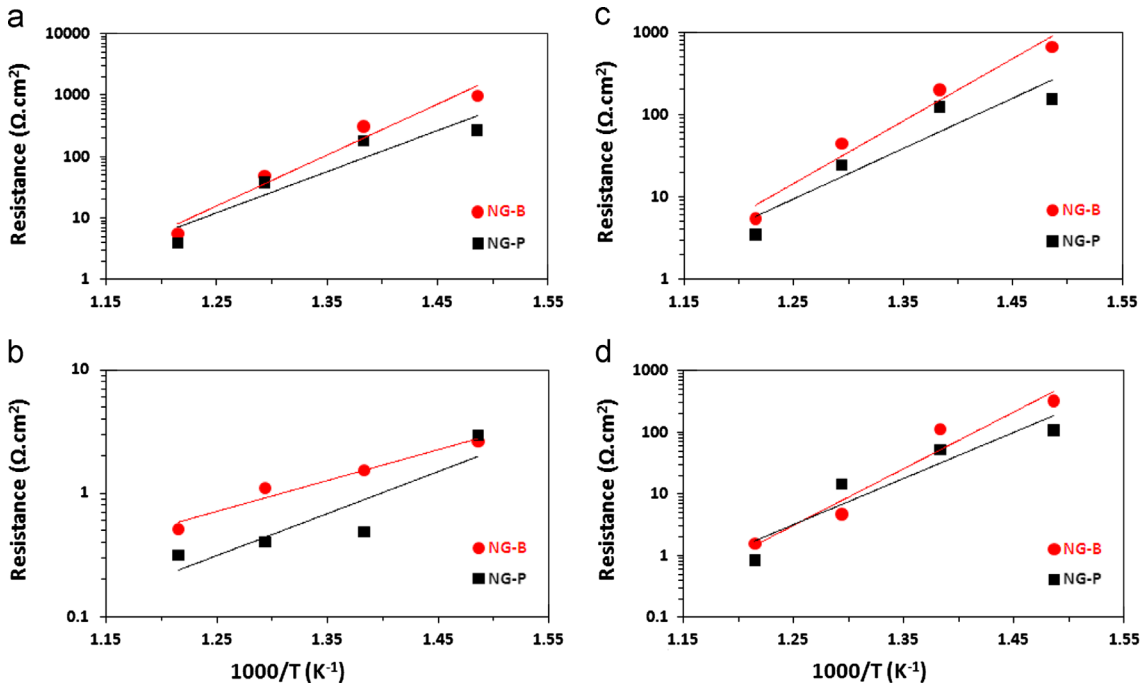

Fig. 8. Arrhenius plot of anode polarization resistance related to (a) R_a, (b) $R_{H'}$, (c) R_H and (d) R_L for the H_2 oxidation reaction on the Ni/GDC cermet anodes of NG-B and NG-P.

Table 6
Activation energies of R_a, $R_{H'}$, R_H, and R_L, for the H_2 oxidation reaction on the NG-B and NG-P anodes.

Specimen	Activation energy (eV)			
	R_a	$R_{H'}$	R_H	R_L
NG-B anode	1.65	0.50	1.50	1.82
NG-P anode	1.33	0.68	1.21	1.49

reaction, and also charge transfer and dissociation/adsorption/diffusion processes on the NG-P cermet anode was observed which could be attributed to the refinement of microstructure on the anode polarization resistance.

Acknowledgments

This project was supported by Materials and Energy Research Center (MERC) of Iran and also in some part by the Pohang University Science and Technology (POSTECH) of South Korea.

References

[1] B.C.H. Steele, Appraisal of Ce1–yGdyO2–y/2 electrolytes for IT-SOFC operation at 500 °C, Solid State Ionics 129 (1–4) (2000) 95–110.
[2] V. Sharma, Q. Liu, R. Sharma, P.A. Crozier, In situ nanostructural changes in Ni–GDC anode for solid oxide fuel cells observed using an environmental transmission electron microscope, Microscopy and Microanalysis 18 (2) (2012) 1128–1129.
[3] T. Ishihara, T. Shibayama, H. Nishiguchi, Y. Takita, Nickel–Gd-doped CeO_2 cermet anode for intermediate temperature operating solid oxide fuel cells using $LaGaO_3$-based perovskite electrolyte, Solid State Ionics 132 (3–4) (2000) 209–216.
[4] A. Faes, A. Hessler-Wyser, A. Zryd, J. Van herle, A review of redox cycling of solid oxide fuel cells anode, Membranes 2 (2012) 585–664.
[5] V. Šepelák, S. Bégin-Colin, G. Le Caër, Transformations in oxides induced by high-energy ball-milling, Dalton Transactions 41 (2012) 11927–11948.
[6] J.A. Aguilar-Martinez, M.B. Hernandez, M.I. Pech-Canul, A.B. Glot, J. Castillo-Torres, A comparative study between the mixed-oxide and high-energy milling planetary method on electrical and microstructural properties for a SnO_2-based ceramic system, Journal of Materials Processing Technology 209 (1) (2009) 318–323.
[7] D. Xu, D. Tang, L. Jiao, H. Yuan, G. Zhao, X. Cheng, Effects of high-energy ball milling oxide-doped and varistor ceramic powder on ZnO varistor, Transactions of Nonferrous Metals Society of China 22 (2012) 1423–1431.
[8] S.W. Zha, W. Rauch, M.L. Liu, Ni–$Ce_{0.9}Gd_{0.1}O_{1.95}$ anode for GDC electrolyte-based low-temperature SOFCs, Solid State Ionics 166 (3–4) (2004) 241–250.
[9] C. Ding, H. Lin, K. Sato, T. Hashida, Synthesis of NiO–$Ce_{0.9}Gd_{0.1}O_{1.95}$ nanocomposite powders for low-temperature solid oxide fuel cell anodes by co-precipitation, Scripta Materialia 60 (2009) 254–256.
[10] B. Rösch, H. Tu, A.O. Störmer, A.C. Müller, U. Stimming, Electrochemical characterization of Ni–$Ce_{0.9}Gd_{0.1}O_{2-\delta}$ for SOFC anodes, Solid State Ionics 175 (2004) 113–117.
[11] C.J. Fu, S.H. Chan, Q.L. Liu, X.M. Ge, G. Pasciak, Fabrication and evaluation of Ni–GDC composite anode prepared by aqueous based tape casting method for low temperature solid oxide fuel cell, International Journal of Hydrogen Energy 35 (2010) 301–307.
[12] C. Fu, X. Ge, S.H. Chan, Q. Liu, Fabrication and characterization of anode-supported low-temperature SOFC based on Gd-doped ceria electrolyte, Fuel Cells 12 (3) (2012) 450–456.
[13] Y. Lee, D.Y. Kim, G.M. Choi, $GdBaCo_2O_{5+x}$ cathode for anode-supported ceria SOFCs, Solid State Ionics 192 (2011) 527–530.
[14] H.J. Cho, G.M. Choi, Effect of milling methods on performance of Ni–Y_2O_3-stabilized ZrO_2 anode for solid oxide fuel cell, Journal of Power Sources 176 (2008) 96–101.
[15] B. de Boer, M. Gonzalez, H.J.M. Bouwmeester, H. Verweij, The effect of the presence of fine YSZ particles on the performance of porous nickel electrodes, Solid State Ionics 127 (2000) 269–276.

[16] H.N. Kim, H.J. Park, G.M. Choi, The effect of alumina addition on the electrical conductivity of Gd-doped ceria, Journal of Electroceramics 17 (2006) 793–798.
[17] J.H. Joo, G.M. Choi, Micro-solid oxide fuel cell using thick-film ceria, Solid State Ionics 180 (2009) 839–842.
[18] Y. Lee, J.H. Joo, G.M. Choi, Effect of electrolyte thickness on the performance of anode-supported ceria cells, Solid State Ionics 181 (2010) 1702–1706.
[19] G.K. Williamson, W.H. Hall, X-ray line broadening from filed aluminum and wolfram, Acta Metallurgica 1 (1953) 22–31.
[20] M.R. Notis, R.M. Spriggs, W.C. Hahn Jr., Elastic moduli of pressure-sintered nickel oxide, Journal of Geophysical Research 76 (29) (1971) 7052–7061.
[21] Dan Jia, Aixi Zhou, Yang Ling, Ke An, A.D. Stoica, Xun-Li Wang, Effect of porosity on the mechanical properties of YSZ/NiO composite anode materials, World Journal of Engineering 7 (3) (2010) 489 ⟨http://wjoe.hebeu.edu.cn/⟩.
[22] A. Nakajo, J. Kuebler, A. Faes, U.F. Vogt, H.J. Schindler, L.-K. Chiang, S. Modena, J. Van herle, T. Hocker, Compilation of mechanical properties for the structural analysis of solid oxide fuel cell stacks. Part I. Constitutive materials of anode-supported cells, Ceramics International 38 (2012) 3907–3927.
[23] M. Moria, E. Sudab, B. Pacaudb, K. Muraic, T. Morigac, Effect of components in electrodes on sintering characteristics of $Ce_{0.9}Gd_{0.1}O_{1.95}$ electrolyte in intermediate-temperature solid oxide fuel cells during fabrication, Journal of Power Sources 157 (2) (2006) 688–694.
[24] Y. Zhang, C. Xia, M. Ni, Simulation of sintering kinetics and microstructure evolution of composite solid oxide fuel cells electrodes, International Journal of Hydrogen Energy 37 (4) (2012) 3392–3402.
[25] C. Metcalfe, O. Kesler, T. Rivard, F. Gitzhofer, N. Abatzoglou, Connected three-phase boundary length evaluation in modeled sintered composite solid oxide fuel cell electrodes, Journal of the Electrochemical Society 157 (2010) B1326–B1335.
[26] Z.Z. Fang, H. Wang, X. Wang, V. Kumar, Grain growth during sintering of nanosized particles, in: R.K. Bordia, E.A. Olevsky (Eds.), Advances in Sintering Science and Technology: Ceramic Transactions, John Wiley & Sons Inc., Hoboken, NJ, USA, 2010, pp. 389–400.
[27] C.K. Blakely, S.R. Bruno, Z.J. Baum, V.V. Poltavets, Effects of ball milling and thermal annealing on size and strain of ASnO3 (A = Ba, Sr) ceramics, Solid State Sciences 15 (2013) 110–114.
[28] T. Ungár, Characterization of nanocrystalline materials by X-ray line profile analysis, Journal of Materials Science 42 (5) (2007) 1584–1593.
[29] A. Faes, Q. Jeangros, J.B. Wagner, T.W. Hansen, J. Van herle, A. Briss, R. Dunin-Borkowski, A. Hessler-Wyser, In situ reduction and oxidation of nickel from solid oxide fuel cells in a transmission electron microscope, ECS Transactions 25 (2) (2009) 1985–1992.
[30] C. Ding, H. Lin, K. Sato, T. Kawada, J. Mizusaki, T. Hashida, Improvement of electrochemical performance of anode-supported SOFCs by NiO–$Ce_{0.9}Gd_{0.1}O_{1.95}$ nanocomposite powders, Solid State Ionics 181 (2010) 1238–1243.
[31] V.M. Janardhanan, V. Heuveline, O. Deutschmann, Three-phase boundary length in solid-oxide fuel cells: a mathematical model, Journal of Power Sources 178 (2008) 368–372.
[32] Z.-P. Li, T. Mori, G.J. Auchterlonie, J. Zou, J. Drennan, Superstructure formation and variation in Ni–GDC cermet anodes in SOFC, Physical Chemistry Chemical Physics 13 (2011) 9685–9690.
[33] A. Kremenovic, B. Antic, M. Vucinic-Vasic, M. Ristic, B. Jancar, J. Rogan, NiO/Ni nanocomposite (micro)structure evolution induced by thermal annealing and milling, Acta Crystallographica A67 (2011) C323–C324.
[34] D.K. Niakolas, M. Athanasiou, S.G. Neophytides, S. Bebelis, characterization and carbon tolerance of new Au– Mo–Ni/GDC cermet powders for use as anode materials in methane fuelled SOFCs, ECS Transactions 35 (2011) 1329–1336.
[35] A. Babaei, S.P. Jiang, J. Li, Electrocatalytic promotion of palladium nanoparticles on hydrogen oxidation on Ni/GDC anodes of SOFCs via spillover, Journal of the Electrochemical Society 156 (9) (2009) B1022–B1029.
[36] Y.J. Kang, G.M. Choi, The effect of alumina and Cu addition on the electrical properties and the SOFC performance of Gd-doped CeO_2 electrolyte, Solid State Ionics 180 (2009) 886–890.
[37] A. Fernandez Zuvich, A. Caneiro, C. Cotaro, A. Serquis, Preparation and characterization of anodes for intermediate temperature solid oxide fuel cells, Procedia Materials Science 1 (2012) 628–635.
[38] I. Epelboin, C. Gabrielli, M. Keddam, H. Takenouti, A model of the anodic behaviour of iron in sulphuric acid medium, Electrochimica Acta 20 (1975) 913–916.
[39] K.B. Yoo, G.M. Choi, Performance of La-doped strontium titanate (LST) anode on $LaGaO_3$-based SOFC, Solid State Ionics 180 (2009) 867–871.
[40] A. Babaei, S.P. Jiang, Analysis of fuel oxidation reaction steps in Ni/GDC anode electrode of solid oxide fuel cells by using palladium nanoparticles, in: Proceedings of SPIE 7743, Southeast Asian International Advances in Micro/Nanotechnology, 77430F, May 19, 2010, http://dx.doi.org/10.1117/12.863029.
[41] J.L.M. Rupp, A. Infortuna, L.J. Gauckler, Thermodynamic stability of gadolinia-doped ceria thin film electrolytes for micro-solid oxide fuel cells, Journal of the American Ceramic Society 90 (6) (2007) 1792–1797.